J Indian Inst. Sci., July–Aug 1990, **70**, 357–393.

IISc THESES ABSTRACTS

Thesis Abstract (Ph.D.)

Experimental and analytical studies on waste heat recovery from the exhaust of a small high speed diesel engine by V. S. Susarla.
Research supervisors: K. Narayanaswamy and M. A. Tirunarayanan.
Department: Mechanical Engineering.

1. Introduction

Because of acute shortage of electrical power in many parts of India, there is a big demand by industry for setting up captive diesel-generating power plants of small to medium output. The thermal efficiency of these units is generally in the range of 25 to 40% depending on the type of engine and the load factor. From the point of view of conserving energy and making the best use of scarce fuel resources, it is evident that there is a large-scale wastage of energy when one uses a diesel generator set. There is, thus, a compelling need to have a closer look at waste heat-recovery systems and their characteristics.

Waste heat can be recovered from the engine coolant, lubricating oil as well as from the exhaust gases. The energy thus recovered is generally used for space and process heating. In turbocharged engines a portion of the energy in the exhaust is utilized to drive the supercharger with resulting gains in power output and economy. The data available in the literature about waste heat recovery refers to large engine systems and give information regarding the range of exhaust gas temperature, and the rate of generation of steam or hot water per unit of power output. Such data are not available for engines of output less than 1,000 kW.

2. Objectives

The present investigation had a two-fold objective. Firstly, it was intended to obtain some data on exhaust heat recovery under varying operating conditions from experiments on a small diesel engine (about 10 kW). Secondly, the system comprising the engine and its heat-recovery unit was to be subjected to thermodynamic analysis for arriving at a better understanding of the manner in which various operating parameters would influence the rate of heat recovery, the effectiveness and the entropy generation.

3. Experimental set-up and results

For the experimental work, a small, high-speed aircooled, direct injection diesel engine rated at 9.8 kW at 2,000 rpm has been used in conjunction with a single pass, counterflow, shell-and-tube type of heat exchanger specially designed and constructed. The heat exchanger is designed to raise saturated steam. Data on the rate of steam generation, the quality of steam and the rate of entropy

generation have been obtained at various engine loads and different pressure levels in the heat exchanger.

The 'mass ratio', *i.e.*, the ratio of the rate of generation of steam to the rate of flow of exhaust gases, is found to be in the range of 0.058 to 0.165 at full load. The reported values for large engines lie in the range of 0.05 to 0.10.

Thermal utilisation *i.e.*, the ratio of the sum of the power output and the exhaust heat recovered to the energy input in the form of fuel is of the order of 40 at 80% engine load.

The heat/power ratio *i.e.*, the ratio of the rate of recovery of exhaust heat energy to the engine output, is about 0.51 at full load. The corresponding value for large engines lies in the range of 0.33 to 0.58.

The heat recovery index (HRI) defined as the ratio of the specific exhaust heat recovered to the specific fuel consumption is maximum when the engine load is between 60 and 80%.

4. A new thermodynamic parameter for waste heat-recovery systems

As a result of the thermodynamic analysis an 'entropy generation parameter' (ENTGEN) has been formulated. It is a dimensionless parameter defined as:

$$\text{ENTGEN} = \frac{\text{Entropy generated in the system per unit time}}{\text{Entropy entering the system per unit time}} = \frac{(\Delta S)_T}{(S_{ig} + S_{iw})}.$$

ENTGEN is believed to be a useful index for comparing the thermodynamic performance of different heat-recovery systems.

5. Conclusions

The value of ENTGEN for the experimental unit lies in the range of 0.40 to 0.59 at full load. The minimum value of ENTGEN is 0.373 for a steam pressure of 2.437 kgf/cm and reached at 80% engine load. For these conditions, the rate of steam generation is 53 kg/h, the mass ratio 0.123, the heat/power ratio 0.47, and the thermal utilisation 39.03%.

References

1. BLAIR, I. M. *et al* — Aspects of energy conservation, *Proc. Summer School*, Lincoln College, Oxford, July 1975, p. 589.
2. BEJAN, A. — The concept of irreversibility in heat exchanger design. Counter flow heat exchangers for gas to gas applications, *Trans. ASME J. Heat Transfer*, 1977, **99**, 374–380.
3. KEENAN, J. H. *et al* — *The fuel shortage and thermodynamics: the entropy crisis*, Thermoelectron Corporation, Waltham, Mass. pp. 455–466.
4. KERN, D. Q. — *Process heat transfer*, McGraw-Hill, 1950.
5. LONDON, A. L. AND SEBAN, R. A. — A generalisation of the methods of heat exchanger analysis, *Inter J. Heat Mass Trans.*, 1980, **23**, 5–16.
6. LONDON, A. L. — Economics and the Second Law: An engineering view and methodology, *J. Heat Mass Trans.*, 1982, **25**, 743–751.

7. LONDON, A. L. *et al* Costs of irreversibilities in heat exchanger design, *Heat Trans. Engng*, 1983, **4**, 59–73.

8. SARANGI, S. AND CHOWDHURY, K. On the generation of entropy in a counterflow heat exchanger, *Cryogenics*, 1982, **22**, 63–65.

Thesis Abstract (Ph.D.)

Prebreakdown conduction and breakdown behaviour of vacuum GAPS under 50 Hz and slow impulse excitations by K. V. Srinivasa.
Research supervisor: G. R. Nagabhushana.
Department: High Voltage Engineering.

1. Introduction

Prebreakdown conduction and breakdown behaviour of vaccum gaps have been extensively studied under dc and submicrosecond excitations. It is only recently that these studies have been carried out under ac and slow impulse excitations and there is considerable scope for improving our knowledge in this area. Further, these studies are of considerable relevance to high voltage–high vacuum devices such as power circuit breakers and triggered vacuum gaps. In view of these, the present work was aimed at studying the prebreakdown conduction and breakdown behaviour in vacuum gaps under 50 Hz and slow impulse excitations.

All the experiments were carried out in vacuum of 10^{-7} Torr or better. Liquid nitrogen trap was used to eliminate contamination (from the oil-diffusion pump). Most of the studies were conducted with stainless steel (Type 304) electrodes. To study the influence of electrode material, OFHC copper and commercial aluminium electrodes have been used. Different electrode shapes were used: plane electrodes (30 mm diameter), hemispheres (3, 5, 10, 15, 20 and 30 mm diameter) and needle electrodes (tip diameter 0.1 mm). The gap configuration involved similar and dissimilar combinations of geometry as well as material. The electrodes were finally polished to mirror finish with 0.3μ alumina powder and ultrasonically cleaned. The gaps were subjected to glow discharge (in H_2) conditioning and/or ac conditioning before the experiments to obtain consistent results.

During prebreakdown current measurements, a compensating circuit was used to bypass gap displacement currents, thus enabling a current measuring sensitivity of 10^{-7} A. This was found to be quite adequate.

2. Results

2.1. *Prebreakdown currents under 50 Hz voltages using stainless steel electrodes*

In conformity with the findings of earlier workers, prebreakdown currents under 50 Hz ac voltages displayed the following features: (i) the current magnitudes were 2 to 3 orders higher, compared to those under comparable dc stresses, (ii) the current peak occurred later than the voltage peak, and (iii) the current waveform was asymmetrical about its own peak causing the F–N plots to be branched. Figure 1 shows typical F–N plots.

Kutty[1] has attributed the above features to: (i) alternating nature of voltage, (ii) anode vapourisation, and (iii) current enhancement due to +ve ions (from anode vapour) causing IF emission. These

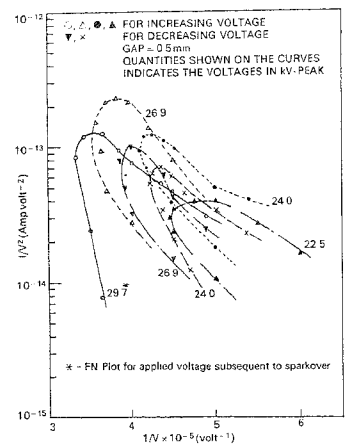

FIG. 1. F–N Plots for symmetrical electrode configurations under 50 Hz ac excitation (30 mm dia. plane–plane).

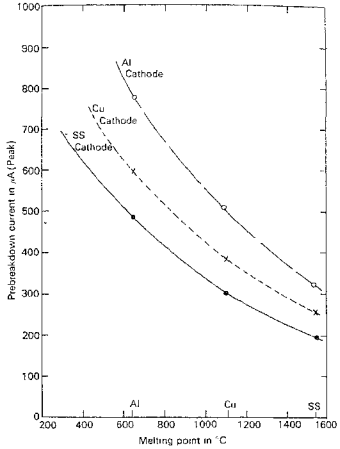

FIG. 2. Variation of prebreakdown current with melting temperature of anode materials of 50 Hz ac excitation

assumptions appear to be very reasonable but the model developed for computation of current wave shape appears to be artificially forced. In the present work, an alternative model, involving IF emission and introducing temporal development, has been proposed. The computed and experimental magnitudes and wave shapes show reasonable agreement and the proposed model is simple and elegant.

Dependence of prebreakdown current on the active area (A_a) of the cathode and anode has been studied and found to obey an equation of the type $I = K \cdot A_a^n$ with n varying from 0.52 to 0.72 depending on A_a itself. Further experiments showed that the anode area has a marginally stronger influence. This dependence is explained on the basis of anode phenomenon and IF emission[2]. Values of β obtained from the initial portion of the F–N plot and based on the IF emission equation are found to be only marginally higher than that of the published values of β for similar gap spacings. This is believed to be a strong support for the proposed mechanism of current enhancement.

2.2. *Influence of electrode material on prebreakdown currents*

This was studied by using stainless steel, OFHC copper and commercial aluminium electrodes. The gap configuration involved similar and dissimilar electrode materials as well as different geometries. The results clearly demonstrate that (i) prebreakdown currents depend strongly on melting point of anode and work function of cathode, (ii) there is a threshold power input for the onset of anode vapourisation—IF emission-based current enhancement, which is dependent almost linearly on the anode melting point, (iii) the delay in the occurrence of current peak is almost linearly related to anode melting point and this results in broader F–N plots, and (iv) β values depend on anode melting point which appears to be a strong evidence of involvement of anode in current enhancement. Figure 2 shows the variation of Pbd current with melting temperature of anode material.

2.3. *Influence of contamination on prebreakdown currents*

Contamination of electrodes gave rise to very high prebreakdown currents but when anode area was negligible (needle electrodes), the prebreakdown currents did not show the peculiar features as described in section 2.1. This shows that high emission currents due to only cathode-based mechanisms is distinctive from current enhancement by anode-based mechanisms. Also, for anode-based mechanisms to be active, significant anode and cathode areas are essential. Thus prebreakdown conduction in vacuum gaps under 50 Hz voltages is a 'volume-phenomenon' rather than in the form of very narrow jets from microscopic emission sites.

2.4. *Prebreakdown currents under impulse excitations of different times to front (200 vs to 5 ms)*

If the assumption that significant anode vapourisation is the root cause of prebreakdown current enhancement under 50 Hz voltages is true, the finite time required (for such vapourisation) may be expected to cause a frequency dependence of prebreakdown currents. As a variable frequency source was not available, prebreakdown currents under slow impulses of times to front in the range 200 μs to 5 ms, the last value corresponding to 50 Hz, were studied.

It was observed that for a given anode material there is a reasonably critical time to front below which the currents are imperceptible indicating the absence of significant current enhancement. Above the critical time to front, the prebreakdown currents displayed all the features peculiar to emission under 50 Hz voltages. Further, the critical time to front was nearly proportional to the melting point of the anode and this confirms the critical role of the anode in current enhancement.

3. Breakdown behaviour under 50 Hz ac and slow impulse excitations

This study was taken up as a logical sequence to the prebreakdown conduction investigations. The experiments were limited to study some salient features only. The results are summarised below.

(i) Under ac voltages, the breakdown voltage (V_b) could be expressed as $V_b = Cd^{\alpha}$ where d is the gap spacing (0.5, 1 and 1.5 mm) and α is a constant (ranges from 0.9 to 1.1).

(ii) Breakdown voltage under 50 Hz ac voltages were comparable with those under dc voltages. Breakdown voltages under impulses were higher than those under 50 Hz voltages by 20 to 30%.

(iii) Breakdown voltages reduce with active area of the electrode under 50 Hz and impulse voltages. The decrease is marginal but the trend is very clear.

(iv) Breakdown voltages are directly proportional to the melting point of the anode material. The value of α, ((i) above), was also higher for anodes of higher melting point. Thus breakdown voltage is essentially due to anode instability.

References

1. KUTTY, K. A. N. — Prebreakdown conduction current measurements in vacuum gaps stressed by ac voltages, *Proc. IEE*, 1976, **23**, 475–476.

2. POROTNIKOV, A. A. AND RODNEVICH, B. B. — IF Emission, *Sov. Phys. Tech. Phys.*, 1978, **23**, 740–741.

Thesis Abstract (Ph.D.)

Investigations of network oxide glasses with novel structural motifs by U. Selvaraj.
Research supervisor: K. J. Rao.
Department: Solid State and Structural Chemistry Unit.

1. Introduction

Simple covalent oxides such as SiO_2, B_2O_3 and P_2O_5 have a pronounced tendency to form glasses[1]. They form extensive two- and three-dimensional networks in which the coordination numbers of network forming atoms (*i.e.* silicon, boron and phosphorus) are typically low (3 or 4). Glasses can also be formed in a binary system of a transition metal oxide and a simple covalent oxide. In these glasses, transition metal ions also participate in the network formation although they have coordination number higher than 4. Phosphomolybdate and phosphotungstate glasses exhibit such novel structural features. They are built of $[MO_{6/2}]$ (M = Mo, W) octahedral and $[PO_{3/2}]$ tetrahedral units. Even though the adaptability of octahedral units in a random network is not in accordance with the well-known Zachariasen's rules[2], they form glasses over a wide range of compositions. We have therefore investigated in detail potassium phosphomolybdate (PPM), potassium phosphotungstate (PPT) and lead phosphomolybdate (LMP) glasses; a new approach to describe such glasses based on phase diagram of structural defects has been developed. We have also studied mixed-alkali diborate glasses using IR spectroscopy and glassy and partially crystalline lithium silicates using magic-angle spinning (MAS) NMR.

2. Experimental

The PPM, PPT and LPT glasses were prepared by melting appropriate quantities of reagent grade K_2CO_3, Pb_3O_4, MoO_3, WO_3 and $(NH_4)_2HPO_4$. Density, microhardness, glass-transition temperature, T_g and change in heat capacity, ΔC_p at T_g were measured by the methods reported elsewhere[3,4]. IR transmission measurements were made on films using a Perkin-Elmer 580 double-beam IR spectrometer. ESR experiments were made on powdered glass samples working in X-band frequency using a Varian E-109 ESR spectrometer. Electronic spectra were recorded on a Hitachi 330 UV-visible near-infrared spectrometer[5]. The effect of temperature and pressure on the electrical conductivity of these glasses was measured as described elsewhere[6,7].

Mixed-alkali borate glass films were prepared from reagent-grade Li_2CO_3, Na_2CO_3, K_2CO_3 and H_3BO_3[8]. Lithium silicate glasses were prepared from reagent-grade Li_2CO_3 and pure acid-washed quartz powder. Partially crystalline lithium silicates were prepared from lithium silicate glass pieces[9,10]. The ^{29}Si MASNMR spectra were obtained with a Bruker CXP-300 solid-state high-resolution spectrometer operating at 59.60 MHz and the samples were spun at 3.5 kHz.

3. Results and discussion

(K_2O, PbO)–MO_3–P_2O_5 [M = Mo, W] systems form glasses over a wide range of compositions. Glasses with compositions, $x(K_2O, PbO)$–$(80 - x)MO_3$–P_2O_5 and $x(K_2O, PbO)$–$(60 - x)MO_3$–P_2O_5 have been chosen for comprehensive characterization studies. Their physical, thermal and spectroscopic properties such as density, molar volume, heat capacity, glass-transition temperature, ESR and IR spectra have been investigated. Variation of Mo^{5+} or W^{5+} concentration as a function of composition has also been studied. The binary phosphomolybdate and phosphotungstate $[MO_3$–$P_2O_5]$ glasses are considered to be made up of random network of corner-shared $[MO_{6/2}]$ octahedral and $[PO_{3/2}]$

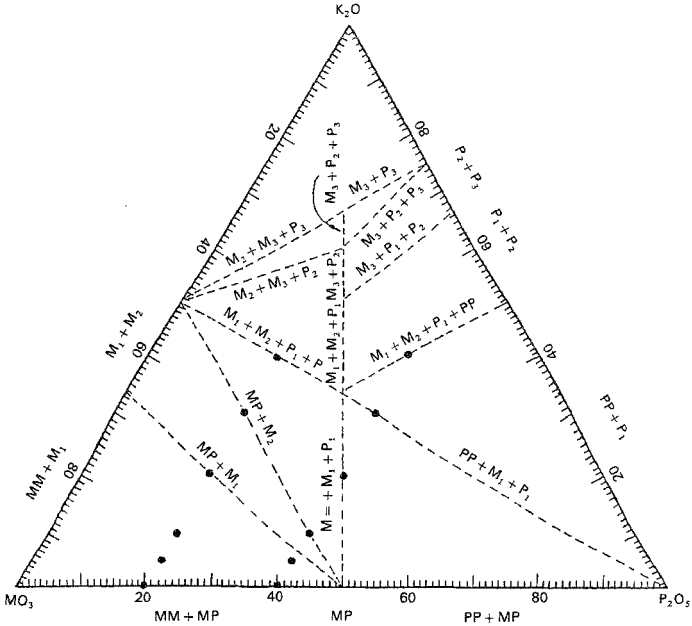

FIG. 1. Structural phase diagram of K_2O–MO_3–P_2O_5 (PPM and PPT) glasses. Structural units present in each region are determined by the units indicated on boundaries Closed circles correspond to composition investigated in this work. $M_1 = [MoO_{5/2}O]^-$, $M_2 = [MoO_{4/2}O_2]^{2-}$, $M_3 = MoO_4^{2-}$, $P = [PO_{3/2}]$, $P_1 = [PO_{2/2}O]^-$, $P_2 = [PO_{1/2}O_2]^{2-}$, $P_3 = PO_4^{3-}$, $MM = [MoO_{6/2}][MoO_{6/2}]$ and $MP = [MoO_{6/2}][PO_{3/2}]_2$.

tetrahedral structural units. Addition of K_2O causes breaking of such a network and as a result, non-bridging (unshared) charged oxygen atoms (structural units or defects) are created. The nature of these structural defects depends on the glass composition and the relative energy of covalent linkages. For example, when the concentration of K_2O is high, the coordination number of molybdenum or tungsten may decrease from 6 to 4 by the formation of MO_4^{2-} discrete anions. Similarly, when the P_2O_5 concentration is high, more number of $[POO_{2/2}O]^-$ defects are created with increasing K_2O concentration. This defect, in particular, has been found to affect profoundly a number of properties of these glasses such as molar volume, glass-transition temperature, high-pressure resistivity variation, etc. All these defects are consolidated into a structural phase diagram (as shown in fig. 1) and in turn are used to rationalize the properties of these complex glass systems[3].

Unlike K_2O, PbO is known to act both as a network former and a modifier in a variety of

conventional glasses. Indeed, it behaves in the same way in phosphomolybdate glasses too. When PbO enters the network, it is presumably present as $[PbO_{4/2}]^{2-}$ structural units causing charge imbalance in the system. However, charge neutrality is achieved in the system by the conversion of $[PO_{3/2}]$ into $[PO_{4/2}]^{+}$ units. On the other hand, when PbO acts as a modifier it behaves in the same manner as K_2O. ESR and IR studies provide strong evidence for the dual structural role of PbO. A structural phase diagram of defects is therefore developed for the ternary $PbO–MoO_3–P_2O_5$ system which also takes into consideration the dual structural role of PbO[4]. The colour of the glasses due to the presence of Mo^{5+} or W^{5+} ions and their stabilization in the glass structure as $[M^5O_{6/2}]^{-}$ $[PO_{4/2}]^{+}$ structural pairs has also been discussed

Electronic spectra of phosphomolybdate and phosphotungstate glasses[5] provide information regarding (i) the extent of distortion of molybdenum or tungsten environment, (ii) the approximate symmetry of structural defects such as $[MoO_{6/2}]$, $[MoO_{5/2}O]^{-}$, $[MoO_{4/2}O_2]^{2-}$, etc., (iii) the Mo^{6+}/Mo^{5+} and W^{6+}/W^{5+} oxidation-reduction potential, (iv) the nature of intervalence transition, and (v) the role of lead in lead phosphomolybdate glasses. ESR spectra of Mo^{5+} and W^{5+} ions[5] indicate that the *d*-electrons are localized on molybdenum and tungsten sites, respectively. The variation of $g_\perp$ and $g_\parallel$ values is consistent with the structural models proposed for these glasses. The change in ESR line width of potassium and lead phosphomolybdate glasses with composition is mainly due to structural modificatons. The line width decreases drastically in lead phosphomolybdate glasses in the region where PbO acts as a network modifier. In all the glasses investigated, $g_\perp$ value is greater than $g_\parallel$ value. Further, the magnitude of $(g_\perp - g_\parallel)$ is larger for glasses containing W^{5+} ions as compared to that of Mo^{5+} ions which is due to the larger spin-orbit coupling constant of W^{5+} ions.

The dc conductivity of phosphomolybdate and phosphotungstate glasses[6] shows that the conductivity of these glasses is due to the hopping of electrons between two valence states (Mo^{5+} to Mo^{6+} or W^{5+} to W^{6+}). In some of the glasses, the activation energy itself is found to be a function of temperature. This appears to be due to thermally activated and variable-range hopping mechnisms operating in different temperature regimes. The relation between conductivity and $[M^{5+}]/[M_{total}]$ (M = Mo, W) ratio does not show any systematic variation. This anomaly can be understood using the structural models of these glasses. On the other hand, Mott's theory and Triberis and Friedman model have been used to obtain conductivity parameters such as percolation distance, R_{ij} and $2\alpha R_{ij}$ (α is a tunneling probability). The conductivity parameter, $2\alpha R_{ij}$ is quite useful to resolve the controversy existing in the literature regarding the tunneling term, $\exp(2\alpha R_{ij})$. For low values of $2\alpha R_{ij}$, it is shown that the $\exp(2\alpha R_{ij})$ term is very significant.

The effect of pressure on the electron transport of potassium phosphomolybdate glasses[7] has indicated that the pressure-induced variation of conductivity in $xK_2O\cdot(80-x)MoO_3\cdot 20P_2O_5$ glasses is somewhat different from that in $xK_2O\cdot(60-x)MoO_3\cdot 40P_2O_5$ glasses. This variation is explained by considering the effect of pressure in perturbing the *d*-levels of various structural defects, $[MoO_{6/2}]$, $[MoO_{5/2}O]^{-}$, $[MoO_{4/2}O_2]^{2-}$, MoO_4^{2-}, etc., present in these glasses. At very high pressure ($\geq$ 50 kbar), the resistivity tends to become independent of pressure for some compositions. These compositions are characterized by the presence of the 2-connected $[PO_{2/2}O]^{-}$ defects.

In $(Li, Na)_2O\cdot 2B_2O_3$ and $(Li, K)_2O\cdot 2B_2O_3$ glass systems, both B–O stretching and B–O–B-bending frequencies exhibit nonlinear shifts, which can be described as a mild mixed-alkali effect[8]. This appears to be due to the influence of mixed $[BO_{3/2}]$ trigonal and $[BO_{4/2}]^{-}$ tetrahedral motifs on mixed-alkali effect. Furthermore, ^{29}Si MASNMR spectra of partially crystalline and glassy lithium silicate have been studied[9,10]. MASNMR provides information regarding the Si–O–Si bond angle distribution with various structural units Q_n (for example, $Q_4 = [SiO_{4/2}]$, $Q_3 = [SiO_{3/2}O]^{-}$, $Q_2 = [SiO_{2/2}O_2]^{2-}$, etc.) present in lithium silicate glasses. It is shown that glasses contain a plurality of structural units with a broad distribution of Si–O–Si bond angles. The width of the distribution appears to be

constant and is characteristic of a particular Q_n species. The full width at half maximum of MASNMR peak of glass is broader than the corresponding crystal. Therefore, an experimental quantification of amorphicity of silicate glasses becomes possible through the agency of MASNMR.

The glasses reported in this thesis are quite novel since they possess mixed octa- and tetrahedral structural motifs in the network. In addition, the structural approach presented here consolidates defects of complex glass systems into structural phase diagrams which are quite useful in understanding their properties.

References

1. RAWSON, H. — *Inorganic glass-forming systems*, 1967, Academic Press.
2. ZACHARIASEN, W. H. — *J. Am. Chem. Soc.*, 1932, **54**, 3841–3851.
3. SELVARAJ, U. AND RAO, K. J. — *J. Non-Crystalline Solids*, 1985, **72**, 315–334.
4. SELVARAJ, U. AND RAO, K. J. — *J. Non-Crystalline Solids*, 1988, **104**, 300–315.
5. SELVARAJ, U. AND RAO, K. J. — *Chem. Phys.*, 1988, **123**, 141–150.
6. RAO, K. J., PARTHASARATHY, G., SELVARAJ, U. AND GOPAL, E. S. R. — *Phys. Chem. Glasses*, 1985, **26**, 101–104.
7. SELVARAJ, U. AND RAO, K. J. — *Phil. Mag.*, 1988, **58**, 203–216.
8. SELVARAJ, U. AND RAO, K. J. — *Spectrochim. Acta*, 1984, **40A**, 1081–1085.
9. SELVARAJ, U., RAO, K. J., RAO, C. N. R., KLINOWSKI, J. AND THOMAS, J. M. — *Chem. Phys. Lett.*, 1985, **114**, 24–27.
10. RAO, C. N. R., THOMAS, J. M., KLINOWSKI, J., SELVARAJ, U., RAO, K. J. AND MILLWARD, G. R. — *Angew. Chem. Int. Ed. Eng.* 1985, **24**, 61–62.

Thesis Abstract (Ph.D.)

Selectivity in photoreactions in cyclodextrin media by M. S. Syamala.
Research supervisors: V. Ramamurthy and S Chandrasekhar.
Department : Organic Chemistry.

1. Introduction

Cyclodextrins (CD) (α, β and γ) (fig. 1) are known to form inclusion complexes with organic substrates and thus provide a microheterogeneous reaction medium for the substrates in aqueous solutions. Alternatively, cyclodextrin complexes are known to exist in the solid state also. Cyclodextrin complexation, both in the solid state and in aqueous solutions, is known[1] to influence the excited-state reactiviy of the included substrate. Modification may be brought about by CD, either in the partitioning of the excited state into various decay modes or intermediate radicals into various modes of recombination. Photo-Fries and photo-Claisen rearrangements have been studied to examine the latter aspect while the photoisomerisation of stilbenes illustrates the former aspect of CD modification.

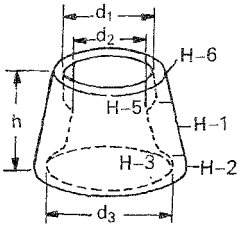

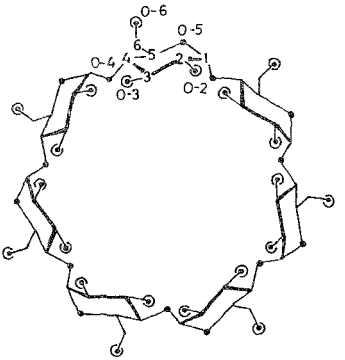

Cyclo-dextrin	d_1 (Å)	d_2 (Å)	d_3 (Å)	h (Å)
α	5.6	4.2	8.8	7.8
β	6.8	5.6	10.8	7.8
γ	8.0	6.8	12.0	7.8

FIG. 1. Shape and structure of cyclodextrin cavity.

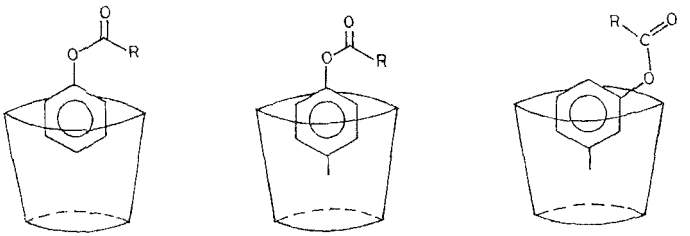

FIG. 2.

2. Molecular traffic control[2,3]

One of the most striking features of CD complexation is the geometrical difference between the complexes of *meta* and *para* isomers of disubstituted aromatic compounds (fig. 2). This has been exploited by Bender[1] and Breslow and coworkers[4] to the full extent in enzyme modelling studies. A remarkable catalysis of the hydrolysis was observed when the *meta*-substituted esters were studied in comparison with the unsubstituted and the *para*-substituted esters. This has been attributed to the orientation of the *meta*-isomer in the CD cavity in a suitable manner that brings the carboxylate moiety in close proximity of the CD hydroxyls to attack. As can be noticed, such a complexation

protects all but one *ortho* position of the aromatic ring from attack by any species. Such a geometrical restriction can control the molecular movement of the attacking reagent. This effect is termed as molecular traffic control. We have succeeded in exploiting this unique feature of CD complexation in the photo-Fries rearrangement of anilides and in the photo-Claisen rearrangement of *meta*-alkoxy phenyl allyl ethers (Scheme 1).

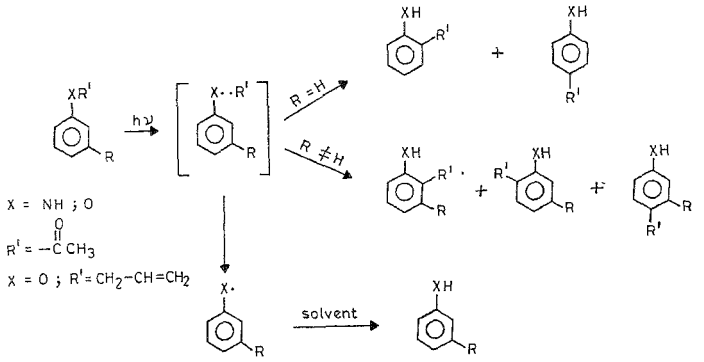

SCHEME 1.

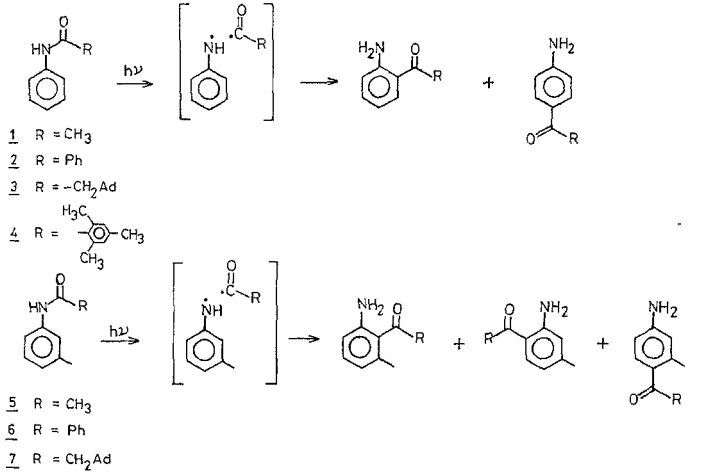

SCHEME 2.

Table I
Results of photolysis of 2

Medium	*ortho*	*para*
Substrate: Benzanilide		
Ethanol	65	35
-CD/H_2O(1.10)	96	4
-CD/solid	100	—

Table II
Results of photolysis of 6

Medium	*ortho*-1	*ortho*-2	*para*
Substrate: 3-Methyl benzanilide			
Ethanol	41.7	41.7	16.6
-CD/H_2O(1:10)	64.0	36·0	—
-CD/solid	100	—	—

The well-known photo-rearrangement of phenyl esters and anilides in organc solvents yields a mixture of *ortho*- and *para*-phenolic or anilinic ketones along with phenol or aniline (Scheme 2). Selective attack of the initially formed acyl radical at the *ortho* position of the aromatic ring, with a complete prohibition of the *para* attack, could be achieved by irradiating substrates **1–4** as their solid β-CD complexes or in aqueous solutions containing an excess of CD. Table I lists the results for **2**. Compounds **5–7** which form a mixture of two *ortho*- and a *para*-rearranged products when photolysed in β-CD revealed a remarkable preference for one among the two *ortho* isomers (Table II). This demonstrates how the traffic of the acyl radical could be regulated towards the only exposed *ortho* position of the aromatic ring in a suitably designed complex (Scheme 3).

A tight fit between the host and the guest molecules could be expected to be necessary to bring about maximum selectivity. Results obtained in the photo-Claisen rearrangement of *m*-alkoxy phenyl allyl ethers highlight the importance of this criterion. Out of the two possible *ortho* isomers and the *para* isomer that are formed during photolysis of **8–12** in organic solvents, only one *ortho* isomer was obtained upon irradiation of the α-CD complexes of these substrates (Scheme 4). The selectivity was found to decrease as the length of the alkyl chain increased (Table III). The β-CD complexes of the same substrates showed an increasing selectivity with the increase in the alkyl chain length. In the case of β-CD the long alkyl chain acts as an intramolecular spacer providing a tight fit between the host and the guest (fig. 3).

3. Restriction on rotational motion[5]

The CD sleeve that surrounds the guest molecule can sterically hinder the rotational motion of an intermediate if it demands a large degree of steric perturbation. An example is seen in the photoisomerisation of stilbenes. Stilbenes undergo facile *trans* to *cis* isomerisation in organic solvents to afford a photostationary state rich (85%) in the *cis* isomer (Scheme 5). Retardation of the *trans* to *cis* isomerisation was observed in aqueous β-CD complexes of stilbenes. In all the cases examined, the *trans* isomer was formed in more than 70% yield. Interestingly the *cis* to *trans* isomerisation proceeded unhindered. This behaviour was in contrast to that of the alkyl cinnamates which behaved in the same manner in β-CD as well as in organic solvents. In the case of *trans*-stilbene the CD wall sterically prevents the 90 twisted intermediate from undergoing further rotation to the *cis* isomer. In the case of cinnamates, the carboxyl moiety of smaller dimensions probably does not experience such hindrance. A different mode of complexation for *cis*-stilbene (Scheme 6) explains its facile isomerisation.

The results of the above investigation expose the fertility of the field of inclusion complexes for further investigation and utilisation to suit the interest of the organic chemist.

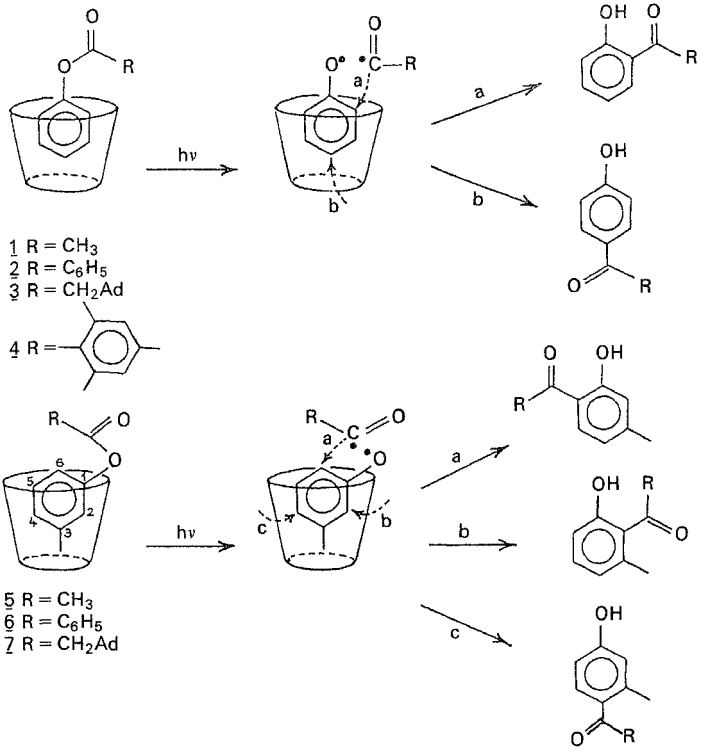
O
O
R
hν
O
O•
•C—R
a
b
a
b
OH
O
R
OH
O
R
1 R = CH3
2 R = C6H5
3 R = CH2Ad
4 R =
R
O
O
6
5
1
2
4
3
hν
R
C
O
a
O
c
b
a
b
c
O
OH
R
OH
R
R
O
OH
O
R
5 R = CH3
6 R = C6H5
7 R = CH2Ad

SCHEME 3.

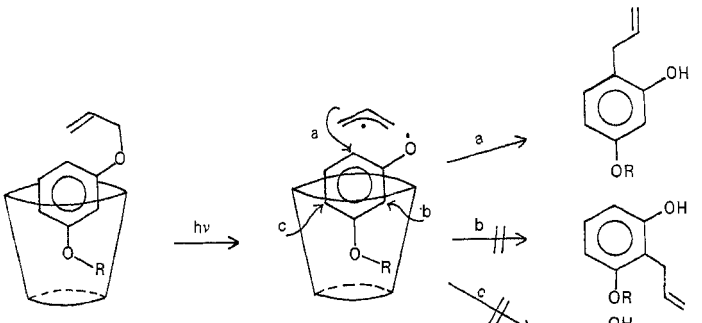

8 R = CH_3
9 R = $(CH_2)_2CH_3$
10 R = $(CH_2)_5CH_3$
11 R = $(CH_2)_7CH_3$
12 R = $(CH_2)_{11}CH_3$

SCHEME 4.

Table III
Results of photolysis of 8–12 in α– and β–CD complexes

α–CD			β–CD		
ortho-2	*ortho*-1	*Substrate*	*ortho*-1	*ortho*-2	*para*
100	—	**8**	62	30	8
95	5	**9**	51	49	—
88	12	**10**	25	75	—
85	15	**11**	10	90	—
65	35	**12**	25	75	—

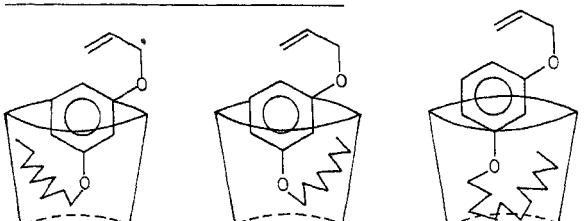

FIG. 3. Structures of β-CD complexes of **10**, **11** and **12**.

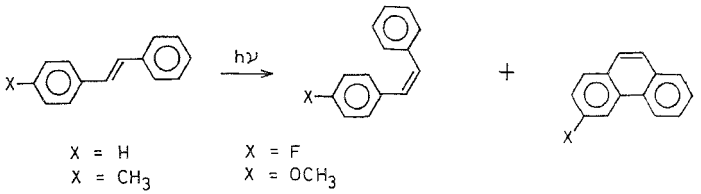

SCHEME 5.

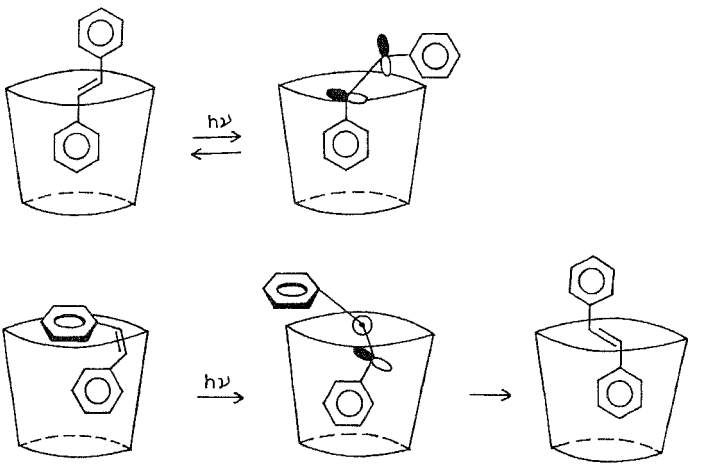

SCHEME 6.

References

1. BENDER, M. L. AND KOMIYAMA, M. D. *Cyclodextrin chemistry*, 1978, Springer-Verlag.
2. NAGESHWAR RAO, B., SYAMALA, M. S. AND RAMAMURTHY, V. *Tetrahedron*, 1988, **44**, 7223–7233.
3. SYAMALA, M. S. AND RAMAMURTHY, V. *Tetrahedron*, 1988, **44**, 7234–7242.
4. BRESLOW, R., CZARNIECKI, M. F., EMERT, J. AND HAMAGUCHI, H. *J. Am. Chem. Soc.*, 1980, **102**, 762–770.
5. SYAMALA, M. S., DEVANATHAN, S. AND RAMAMURTHY, V. *J. Photochem.*, 1986, **34**, 219–229.

Thesis Abstract (Ph.D.)

EXAFS Investigations of supported metal catalysts and other systems by G. Sankar.
Research supervisor: C. N. R. Rao.
Department: Solid State and Structural Chemistry Unit.

1. Introduction

Extended X-ray absorption fine structure (EXAFS) provides valuable structural information related to short-range order in solids[1,2]. Accordingly, interatomic distances and coordination numbers of metal atoms can be obtained immaterial of whether the material is polycrystalline or amorphous. EXAFS is ideally suited for the study of supported metal catalysts which cannot be usefully examined by conventional structural techniques[3]. In this thesis, results of EXAFS investigations of a few important catalysts systems are reported. The catalysts studied are: methanol synthesis Cu–ZnO catalysts, bimetallic Cu–Ni/γ-Al_2O_3 catalysts Co–Mo/γ-Al_2O_3 hydrodesulphurization catalyst and the strong metal-support interaction (SMSI) catalysts, Ni/Nb_2O_5 and Ni/TiO_2. The present investigations have yielded some results of relevance to catalysis and have also enabled certain improvements in the method of analysis of EXAFS data of complex multiphasic systems such as supported metal catalysis.

2. Experimental

Catalyst samples Cu–ZnO[4] (CU:Zn ratio of 10:90, 20:80 and 33:67), Cu–Ni/Al_2O_3[5] (Cu:Ni ratio of 0:100, 25:75, 50:50, 75:25 and 100:0), Co–Mo/γ-Al_2O_3[6] (Co:Mo ratio of 4:12), Ni/TiO_2[7] and Ni/Nb_2O_5[7] (Ni content 10%) were prepared by the procedure described in literature. X-ray absorption spectra were recorded using a bent crystal spectrograph, the analyser being 201 planes of mica crystal. A rotating anode X-ray generator (GX-18 Marconi-Avionics UK Ltd.) and a static anode X-ray generator (Rich Seifert & Co., West Germany) with copper target and molybdenum target were used as sources of X-radiation.

3. Analysis of EXAFS data

The EXAFS data were analysed in the single scattering approximation where the EXAFS function is related to the structural parameters by

$$\chi(k) = (N_j/R_j^2)\exp(-2\sigma_j^2k^2)F_j(k)\,\mathrm{SIN}(2R_jk_j + 2\delta_j(k), \tag{1}$$

where

$$k = (1/\hbar)[2m(E - E_0)]^{1/2}, \tag{2}$$

N_j the number of nearest neighbours of the jth shell, R_j the interatomic distance, σ_j the Debye-Waller term. $F_j(k)$ and $\delta_j(k)$ are the amplitude and phase functions, respectively. The analysis was carried out by extracting the normalized EXAFS data from the raw absorption spectra employing background subtraction using cubic spline fit. The normalized data were Fourier transformed and the region of interest (1.1 to 3.3 Å) was windowed and backtransformed for further curve-fitting analysis.

In the case of multiphasic systems the EXAFS function $\chi(k)$ was defined as

$$\chi_{\mathrm{Total}}(k) = \sum_i x_i\chi(k). \tag{3}$$

Comparing eqns 1 and 3 we find that the N_j and x_i are complementary; consequently, we have

employed fixed N_j values (as obtained from model compounds). The unknown scatterers were determined using residual spectrum method, obtained as the difference between the calculated and experimental EXAFS data. In addition to the above-mentioned analysis, we have employed the logarithmic ratio of the amplitude part of the EXAFS function of the model system and the experimental system for determining the types of back scatterers.

4. Results and discussion

All the catalyst systems studied show the presence of more than one type of neighbour in the region of interest 1.1 to 3.3 Å. The results of a Cu K-edge EXAFS study of calcined catalysts clearly show the presence of two species, Cu^{2+} in a CuO-like phase with a Cu–O distance of 1.99 Å and Cu–Cu distance 3.0 Å and Cu^{2+} in substitutional sites of ZnO lattice accounting for the observed distance of 3.22 Å. The reduced catalysts contain three species Cu^0, Cu^{1+} in a Cu_2O-like phase and Cu^{1+} in an interstitial site of ZnO lattice. The distance of 1.8 Å could be accounted for the Cu_2O-like phase, the distance of 2.56 Å due to a Cu–Cu in Cu metal and the Cu–Cu distance of 2.2 Å could only be accounted for by Cu^{1+} occupying interstitial sites of ZnO lattice.

The Ni K-edge EXAFS reveal the presence of Ni^0 as well as Ni^{2+}, the latter in both octa- and tetrahedral environments in γ-Al_2O_3; copper is present as Cu metal and as a Cu_2O-like phase. The concentration of Ni^0 relative to Cu^{1+} increases with the proportion of nickel. These results are also confirmed by X-ray photoelectron spectroscopy and Auger electron spectroscopy. On the basis of the concentration of phases and interatomic distance obtained from the EXAFS analysis of multiphasic systems we suggest the formation of alloy-like phase (CuNi alloy) other than the pure metallic phase. The study clearly shows the promotional effect of Ni^{2+} on Cu/γ-Al_2O_3 and Cu^{2+} on Ni/γ-Al_2O_3.

Mo K-edge EXAFS studies of the sulphided Co–Mo/γ-Al_2O_3 hydrodesulphurization catalyst (Co:Mo ratio of 4:12) show that Mo is present as a sulphidic species similar to MoS_2 with a particle size of 17 Å. The analysis of the Co K-edge EXAFS data shows two types of coordination, one with six sulphurs (but not as a bulk sulphide) and the other with four oxygens. The partially sulphided Co atoms are linked to oxygen atoms of the octahedral sites of γ-Al_2O_3 thereby stabilizing the small MoS_2 particles and also anchor them to the γ-Al_2O_3 lattice.

Ni K-edge EXAFS studies of the strong metal-support interaction (SMSI) catalysts, Ni/Nb_2O_5 catalyst reduced at 300°C shows a metallic phase and an oxidic phase. On reducing the catalysts as 500°C, the EXAFS analysis clearly demonstrated the presence of a long Ni...Nb (Ni...Ti) distance of 3.2 Å and short Ni–Nb (Ni–Ti) distance of 2.65 Å. Comparing the results obtained on the catalysts reduced at 300°C and 500°C, we find that there is considerable structural reorganization of the support oxide in the vicinity of the Ni particles.

X-ray absorption near edge structure (XANES) and EXAFS studies of several model compounds, copper glucuronates and copper complex formed from the *Pseudomonas aeruinosa* were carried out. The study clearly shows the presence of square-planar coordination in the copper complex formed *Pseudomonas aeruginosa* with the Cu–O distance close to that in cupric glucuronates and cupric acetylacetonate. EXAFS has been shown to be useful for studying the metal–metal bonding in copper carboxylates.

In addition to EXAFS studies of catalysts and copper compounds, XANES studies of mixed valent oxides were carried out. The transition energies of $1s \rightarrow 3d$, $1s \rightarrow 4s$ and $1s \rightarrow 4p$ were found to vary parabolically as a function of q, the effective atomic charge. Similarly the energy difference $3d$–$4p$ and $3d$–$4s$ obtained from the XANES also shows a similar variation with respect to q.

References

1. PARTHASARATHY, R., SARODE, P. R., RAO, K. J. AND RAO, C. N. R. — *Proc. Indian Natn. Sci. Acad.*, 1982, **48A**, 119–143.
2. RAO, C. N. R. AND GOPALAKRISHNAN, J. — *New directions in solid state chemistry*, 1986, Cambridge Solid State Science Series, Cambridge University Press.
3. SINFELT, J. H., VIA, G. H. AND LYTLE, F. W. — *Catalysis Rev. Sci. Engng*, 1984, **26**, 81–140.
4. HERMAN, R. G., KLIER, K., SIMMONS, G. W., FINN, B. P., BULKO, J. B. AND KOBLYLINSKI, T. P. — *J. Catalysis*, 1979, **56**, 407–429.
5. HIERL, R., KNOZINGER, H. AND URBACH, H. P. — *J. Catalysis*, 1981, **69**, 475–486.
6. SANKAR, G., SARODE, P. R., SRINIVASAN, A., RAO, C. N. R., VASUDEVAN, S AND THOMAS, J. M. — *Proc. Indian Acad. Sci. (Chem. Sci.)*, 1984, **93**, 321–334.
7. KO, E. I., HUPP, J. M., ROGAN, F. H. AND WAGNER, N. J. — *J. Catalysis*, 1983, **84**, 85–94.

Thesis Abstract (Ph.D.)

Acid-catalysed cyclisation of steroidal seco-diones. Total synthesis of racemic copacamphor and ylangocamphor and their C_1-homologues by R. Chandra.
Research supervisor: T. R. Kasturi.
Department: Organic Chemistry.

1. Introduction

In the field of natural products, the chemistry of diterpenes (C_{20} units) and sesquiterpenes (C_{15} units) is extensively studied. A large number of these terpenes possess the bicyclo[3.2.1]octane ring system as a structural subunit. Various synthetic challenges involved in the construction of the framework are reported in literature[1,2]. The synthesis of copacamphor, ylangocamphor, their C_1-homologues and a bicyclo[3.2.1]octane intermediate is reported in this thesis.

2. Experimental

The syntheses of tricyclic hydroxy ketones **2b** and **2d** and the bicyclo[3.2.1]octan-6,8-dione **3b**, **3d** and **4b** have been achieved by acid-catalysed cyclisation of the seco-dione **1b** and **1d**. Condensation of 2-ethylcyclopentan-1,3-dione with the vinyl carbionl obtained by Grignard reaction of 2′,3,4′-trimethoxypropiophenone with vinylmagnesium bromide gave 2-ethyl-2[3-(2,4-dimethoxyphenyl)-5-methoxypent-2-enyl]-cyclopentan-1,3-dione (seco-dione **1b**). Treatment of the seco-dione **1b** with anhydrous methanolic hydrogen chloride yielded the two isomeric diketones and tricyclic hydroxy ketone. Based on the PMR, IR and mass spectal data, isomeric *exo* and *endo* structures have been assigned to these diketones. Structure **2b** has been assigned to the tricyclic hydroxy ketone on the basis of its PMR and IR spectra and in analogy with the earlier reported compounds[3] **2a** and **2c**. Similarly, methanolic hydrogen chloride reaction of the seco-dione **1d** gave the *endo* diketone **3d** and the tricyclic hydroxy ketone **2d**.

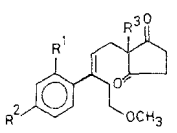

1

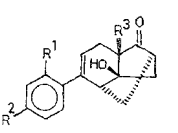

2

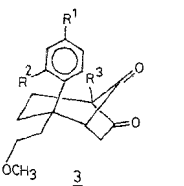

3

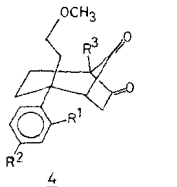

4

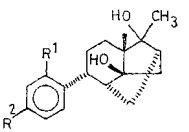

5

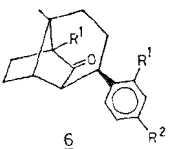

6

(a) $R^1 = R^2 = OCH_3$; $R^3 = CH_3$
(b) $R^1 = R^2 = OCH_3$; $R^3 = C_2H_5$
(c) $R^1 = H$; $R^2 = OCH_3$; $R^3 = CH_3$
(d) $R^1 = H$; $R^2 = OCH_3$; $R^3 = C_2H_5$

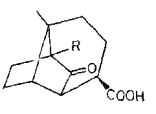

7

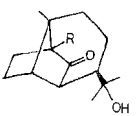

8

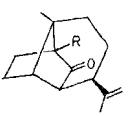

9

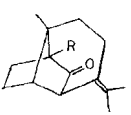

10

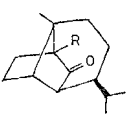

11

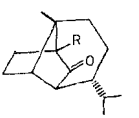

12

(e) R = CH_3 (f) R = C_2H_5

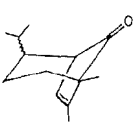

13

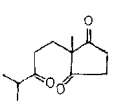

14

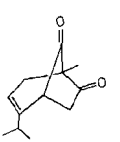

16

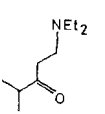

15

A stereospecific rearrangement of the homobrendane system to the perhydro-1,4-methano-indene system has been achieved in three steps. Catalytic hydrogenation of the tricyclic hydroxy ketone followed by Grignard reaction with methylmagnesium idodide afforded the diol **5a** in more than 90% yield. Refluxing the diol with a catalytic amount of *p*-toluenesulfonic acid in benzene or brief treatment with BF_3–Et_2O provided exclusively a tricyclic ketone. Similar compounds were obtained in the reaction of the diols **5b–d** with *p*-TsOH or BF_3–Et_2O. Structure **6** was assigned to these tricyclic ketones on the basis of their IR, NMR and mass spectra. X-ray structure analyses of the tricyclic ketone **6a** and **6d** further confirmed the assigned structure[4].

This rearranged ketone **6a** has been converted to the natural product precursor (±)-copacamphor **11e**[5–7] and its C_5-epimer ylangocamphor **12e**. Oxidation of the aromatic compound with RuO_4 generated *in situ*[8] afforded the acid **7e** which on esterification followed by Grignard reaction with methylmagnesium iodide yielded the tert. alcohol **8e**. Dehydration of the alcohol gave a mixture (7:3) of olefins **9e** and **10e**. Hydrogenation of the mixture of olefins and further separation afforded (±)-copacamphor and (±)-ylangocamphor which showed spectral characteristics identical to those of authentic samples[9,10]. Following the same methodology, (±)-C_1-homocopacamphor **11f** and (±)-C_1-homoylangocamphor **12f** have been synthesised from the tricyclic ketone **6d**.

A convenient and efficient preparation of the strategic intermediate **13** which has been utilised in the synthesis of a number of sesquiterpenes of copa and ylango series has been achieved. Acid-catalysed cyclisation of the triketone **14** obtained by the condensation of the amino compound **15** with 2-methyl-cyclopentan-1,3-dione yielded the bicyclo[3.2.1]oct-2-en-6,8-dione **16** which was transformed in five steps to the desired intermediate **13.**

References

1. APSIMON, J. (ed.) — *Total synthesis of natural products*, 1983, **5**, pp. 471–488, Wiley.
2. MAURITS VANDEWALLE AND PIERRE DE CLERCQ — *Tetrahedron*, 1985, **41**, 1767–1831.
3. KASTURI, T. R. AND RAMACHANDRA, R. — *Indian J. Chem.*, 1975, **13**, 9–12.
4. KASTURI, T. R., RAMAL CHANDRA, RAMACHANDRA, R., MADHAVA REDDY, S, VENKATESAN, K., SRIKRISHNAN, T., GURU ROW, T. N., PURANIK, V. G. AND TAVALE, S. S. — *J. Chem. Soc., Chem. Commun.*, 1987, 75–76.
5. WESTFELT, L. — *Acta Chem. Scandinavica*, 1966, **20**, 2829–2840.
6. KOLBE, M. AND WESTFELT, L. — *Acta Chem. Scandinavica*, 1967, **21**, 585–587.
7. KOLBE-HAUGWITZ, M. AND WESTFELT, L. — *Acta Chem. Scandinavica*, 1970, **24**, 1623–1630.
8. CARLSEN, PER H. J., KATSUKI, T., MARTIN, V. S. AND BARRY SHARPLESS, K. — *J. Org. Chem.*, 1981, 3936–3938.
9. HODGSON, G. L., MACSWEENEY, D. F. AND MONEY, T. — *Tetrahedron Lett.*, 1972, 3683–3686.
10. HODGSON, G. L., MACSWEENEY, D. F. AND MONEY, T. — *J. Chem. Soc., Perkin Trans. I*, 1973, 2113–2130.

Thesis Abstract (Ph.D.)

Syntheses of some terpenic and other natural products of plant and marine origin by A. Sudalai.
Research supervisor: G. S. Krishna Rao.
Department: Organic Chemistry.

1. Introduction

Monoterpenes (C_{10}-isoprenoids) are widely used in flavor and perfume industries because of their attractive odors, low molecular weights and high volatilities. Many sesquiterpenes (C_{15}-isoprenoids) are important constituents of the characteristic aromas of plant products and many others exhibit interesting physiological properties. These groups of naturally occurring substances, containing ten and 15 carbon atoms and derivable biogenetically from mevalonic acid *via* geranyl and farnesyl pyrophosphates, respectively, offer a truly remarkable structural variety and synthetic targets for the organic chemist. The syntheses of several such naturally occurring terpenoids are reported in this thesis.

2. Monoterpenoids

Four monoterpenoids, **2** and **3**, occurring[1] in the plant *Calea pilosa*, and **5** and **6**, occurring[2] in *Molopospermum peloponnesiacum* have been synthesized. Oxidation of diol **1**, concurrently with dehydration, proceeded smoothly with active MnO_2 to furnish **3**. Treatment of **4** with *p*-toluenesulphonic acid gave **2**. Single-step degradation by ozonolysis of the bisnorsesquiterpenic unsaturated ketone **19** produced the monoterpenic aldehyde **5** which on silver-oxide oxidation afforded the acid **6**.

3. Meroterpenoids

The synthesis of two meroterpenoids **8**, isolated[3] from *Senecio graveolens* and **7**, isolated from *Helianthella uniflora*[4] and *Senecio amplexicaulis*[5] has been achieved. Sodium borohydride reduction of **10** gave **11** which was converted to the triol **9** using MeMgI in refluxing xylene[6]. Oxidation of **9** with active MnO_2 gave **8**. Treatment of **12** with *p*-toluenesulphonic acid afforded **7**.

4. Sesquiterpenoids

The synthesis of four sesquiterpenoids **17**, occurring in *Laurentia nidifica*[7] and *L. intricata*[8], **18**, its dehydroanalogue, acetyldehydrorishitinol **22**, isolated from potatoes and **29**, isoparvifolin has been achieved. Ozonolysis of **13** gave **14** which was reduced to diol **15**. Metal-ammonia reduction[10] of **15**, followed by oxidation with Jones reagent furnished **16**. Selective monobromination of **16** at the α-methylene position was achieved using pyridinium bromide perbromide[11] to give **20** which was dehydrobrominated to give **19**. Grignard reaction of **16** and **19** with excess vinylmagnesium bromide generated the sesquiterpene alcohols **17** and **18**, respectively.

Dehydrogenation of **23** with DDQ yielded **26**, which was converted to the alcohol **27**. Jones oxidation of **27** produced the ketone **25** which was also prepared by acetylation of **24** obtained from **28** under Friedel-Crafts conditions. Lithium-liquid ammonia reduction[10] of **25** in the presence of $Fe\,Cl_3$ gave **21** which was transformed in one step to the natural product **22** with a tertiary acetate function, using excess Me–MgI followed by quenching with acetic anhydride and sodium acetate.

The methoxy acid **31**, prepared from **33** and **34** involving several steps, was cyclized with polyphosphoric acid to give **32**. Borohydride reduction of **32** gave the corresponding secondary

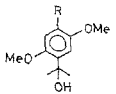

1. R = CH_2OH
4. R = Me

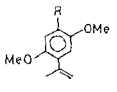

2. R = Me
3. R = CHO

5. R = CHO
6. R = COOH

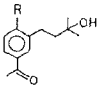

8. R = OH
12. R = OMe

7

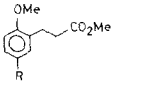

10. R = $COCH_3$
11. R = $CHOHCH_3$

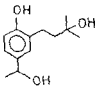

9

13

14. R = CHO
16. R = CH_3

15

19

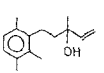

17

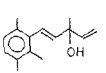

18

20

21

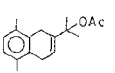

22

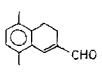

23

28

24. R=H
25. R=$COCH_3$
26. R=CHO
27. R=$CHOHCH_3$

29. R'=CH_3, R=OH
30. R'=CHO, R=OMe

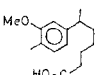

31

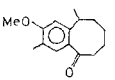

32

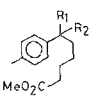

33. R_1,R_2=O
34. R_1=H,R_2=Me

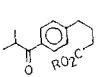

35

36

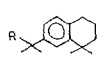

37. R = CH_3
38. R = $CO_2CH_2CH_3$
39. R = CH_2OH
40. R = CHO

41. R^1=CHO, R^2=OH, R^3=Br
42. R^1=CHO, R^2=OH, R^3=H
43. R^1=CHO, R^2=Br, R^3=H

44. R^1=CH_2OH, R^2=OH, R^3=Br
45. R^1=CH_2OH, R^2=OH, R^3=H
46. R^1=CH_2OH, R^2=Br, R^3=H

alcohol which under Vilsmeier reaction conditions[12] produced the aldehyde **30**. Wolff-Kisher reduction of **30** gave **29** which was demethylated with BBr_3 to furnish isoparvifolin **29**, a double-bond isomer of parvifolin, a naturally occurring sesquiterpene[13], with a novel skeleton.

5. 7-*t*-Butyl-1,1-demethyltetralin

The synthesis of 7-*t*-butyl-1,1-dimethyltetralin **37**, a rearrangement product of 10-methylenelongibornane[14], has been achieved starting from the keto ester **35**. The ketone **36** obtained from **35** in three steps was converted to **38** using lead tetraacetate and triethyl orthoformate[15]. The ester function in **38** was converted to the methyl group by the standard sequence of reactions (**38** → **39** → **40** → **37**).

6. Bromophenols

The synthesis of six bromophenols (**41** to **46**), metabolites isolated[16] from marine algae has been achieved. Vanillin served as the starting material for the syntheses of **41**, **42**, **44** and **45**. For compounds **43** and **46** *p*-cresol served as the starting material.

References

1. METWALLY, M. A. AND KING, R. M. — *Indian J. Chem. (B)*, 1985, **24**, 982.
2. KUBECZKA, K. H. AND ULLMANN, I. — *Phytochemistry*, 1981, **20**, 828–830.
3. LOYOLA, L. A. PEDREROS, S AND MORALES, G. — *Phytochemistry*, 1985, **24**, 1600–1602.
4. BOHLMANN, F. AND GRENZ, M. — *Chem. Ber.*, 1970, **103**, 90–96.
5. BOHLMANN, F. AND ZIESCHE, J. — *Phytochemistry*, 1980, **19**, 2681–2684.
6. CABIDDU, S. — *Ann. Chim. (Rome)*, 1970, **60**, 488–496.
7. SUN, H. H., WARASZKIEWICZ, S. M. AND ERICKSON, K. L. — *Tetrahedron Lett.*, 1976, 585–588.
8. HORSLEY, S. B., CARDELLINA, J. H. AND MEINWALD, J. — *J. Org. Chem.*, 1981, **46**, 5033–5035.
9. ALVES, L. M., KIRCHNER, R. M., LODATO, D. T., NEE, P. B., ZAPPIA, J. M., CHICHESTER, M. L., STUART, J. D., KALAN, E. B. AND KISSINGER, J. C — *Phytochemistry*, 1984, **23**, 537–538.
10. BIRCH, A. J. AND SUBBA RAO, G. S. R. — *Adv. Org. Chem.*, 1972, **8**, 1–65.
11. FREEDMAN, H. H. AND DOORAKIAN, G. A. — *Tetrahedron*, 1964, **20**, 2181–2184.
12. ANANTHA REDDY, P. AND KRISHNA RAO, G. S. — *Indian J. Chem. (B)* 1981, **20**, 100–103.
13. BOHLMANN, F. AND ZDERO, C. — *Chem. Ber.*, 1977, **110**, 468–473.
14. SHITOLE, H. R. AND NAYAK, U. R — *Indian J. Chem. (B)*, 1983, **22**, 215–219.
15. FUJII, K., NAKAO, K. AND YAMAUCHI, T. — *Synthesis*, 1982, 456–457.
16. MANLEY, S. L. AND CHAPMAN, D. J. — *Phytochemistry*, 1980, **19**, 1453–1457.

Thesis Abstract (Ph.D.)

Modification of photochemistry by cyclodextrin complexation: Norrish type I and type II reactions of benzoin derivatives and aryl alkyl ketones by G. Dasharatha Reddy.
Research supervisors: V. Ramamurthy and K. Venkatesan.
Department: Organic Chemistry.

1. Introduction

The photochemical Norrish type I and type II reactions of cyclodextrin-bound benzoin alkyl ethers (**1–6**), α-alkyl deoxybenzoins (**7–11**) and a series of aryl alkyl ketones (**12–27**) have been investigated both in cyclodextrin aqueous solution and solid complexes. Irradiation of **1–3** in cyclodextrin media leads to large change in product distribution from that found in benzene and methanol. In aqueous solution, type II products compete with type I α-cleavage and in the solid complexes type II products constitute more than 90% of the product distribution. Whereas **4–6** bound to cyclodextrin behaves similarly in aqueous solution to that of **1–3**, it differs drastically in solid complexes *i.e.*, only type I products were formed. The selectivity/sensitivity of the reaction is interpreted as a measure of change in the ground state distribution of reactive and unreactive conformations brought about by cyclodextrin inclusion phenomena and cage effects. Photolysis of α-alkyl deoxybenzoins **7–11** results in the formation of products both from types I and II in homogeneous media as well as in aqueous cyclodextrin complexes. In the solid complexes, **7–11** exclusively gives type II products. Both cyclobutanol and deoxybenzoin were formed. Conformational and super cage effects have been invoked to explain the dramatic alteration in the solid complexes. Finally the effect of cyclodextrin on type II intermediate 1,4-biradical derived from aryl alkyl ketones (**12–25**) have been studied. Results indicate that the cyclisation/cleavage ratio depends only on the chain length but not on the substitution at γ-position or the ring substitution.

The continuing strive of chemists for selectivity in chemical reactions has led to the alteration of chemical properties through host-guest complexation[1–3]. The chemistry of cyclodextrins has occupied a central interest in host-guest phenomenon for the past few decades because of its ability to form inclusion complexes with a great variety of organic compounds and modify one or more reactions is well known. Specificity and selectivity are some of the important characteristics of cyclodextrin catalysis. However, the origin of specificity/selectivity has been scant due to poor information on the structure of the inclusion compounds. We would like to address these questions by studying various complexes of cyclodextrin with **1–25** which undergo Norrish type I and type II reactions.

The photolysis of benzoin alkyl ethers (**1–3**) in solution has been extensively studied and the main details of the reaction have been elucidated[4–7]. They undergo type I α-cleavage upon photolysis to form benzoyl-benzyl radical pair, which subsequently undergoes free radical reaction to give as main products, the pinacol ethers and benzil along with minor amounts of benzaldehyde. γ-Hydrogen abstraction which is the predominant photochemical reaction for α-alkoxy acetophenones (**23–25**) does not compete with the α-cleavage reaction in benzoin ethers (**1–3**), Scheme 1. The absence of potentially feasible type II hydrogen abstraction in these compounds can be either due to the low occupancy of benzoin alkyl ethers in necessary *cis*oid conformation or can be due to inherent high rate and efficiency of the α-cleavage. Cyclodextrin encapsulation, though may not alter the rate of α-cleavage, is expected to increase the probability of recombination of the radical pair generated from α-cleavage leading to decrease in the efficiency of type I α-cleavage. Further, it is probable that benzoin alkyl ethers when included in cyclodextrin could adopt the desired conformation for type II reaction. These two features, we anticipated, would allow a reasonable competition between type

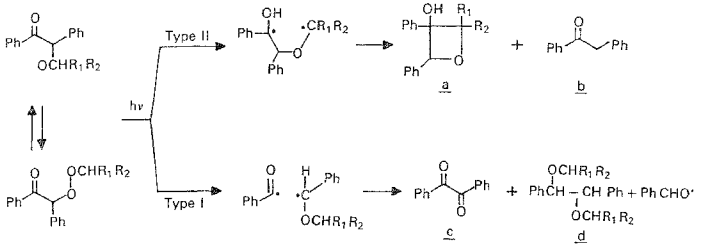

1) $R_1 = R_2 = H$, 2) $R_1 = CH_3$, $R_2 = H$, 3) $R_1 = R_2 = CH_3$

SCHEME 1.

II and type I reactions. The goal of the present investigation is to probe the effect of cyclodextrin in bringing about the conformational and cage effects. Effect of chain length has also been studied with **4–6**. The generality of the reaction in related systems has been demonstrated by **7–12** and the partitioning of the intermediate 1,4-diradical to cyclisation and cleavage were elucidated using compounds **12–25**.

2. Characterisation of the complexes

Addition of **1–3** to saturated aqueous solution of β-cyclodextrin precipitated a white solid. The X-ray powder diffraction of the complex and β-cyclodextrin were compared to check the authenticity of complex formation. In aqueous media the complex formation has been established by their proton NMR spectroscopy and by measuring the dissociation constants. All the compounds investigated here have very high association with β-cyclodextrin and are stable at our experimental condition.

3. Benzoin ethers and related systems

Photolysis of benzoin alkyl ethers (**1–3**) in N_2-saturated benzene and methanol resulted in the formation of benzaldehyde, benzil and an equimolar mixture of diastereomeric pinacol ethers. Solution results are consistent with the literature reports[8–11]. Photolysis in cyclodextrin media resulted in large change in product distribution. In aqueous cyclodextrin solution minor amounts of type II products were also formed. Most significantly, solid cyclodextrin complexes upon photolysis produced >90% of the type II products. The importance of the cyclodextrin cavity in bringing about this remarkable change in photobehaviour of **1–3** is revealed by the following observations. When microcrystalline compounds **1–3** under identical conditions were irradiated they were photostable. Further, irradiation of a mechanical mixture of cyclodextrin and **1–3** did not yield type II products. The proposed mechanism to explain the results has been illustrated in Scheme 2.

Formation of oxetanols and deoxybenzoin under conditions wherein the formation of the atoms is restricted (in the solid complexes) suggests that part of the molecules are included in cyclodextrin with favourable conformation for γ-hydrogen abstraction *i.e.*, conformation *A*. If there is no interconversion between *A* and *B*, as would be expected in the solid complex, the total yield of type II products would reflect ground state distribution of *A* and *B*. The most remarkable observation is

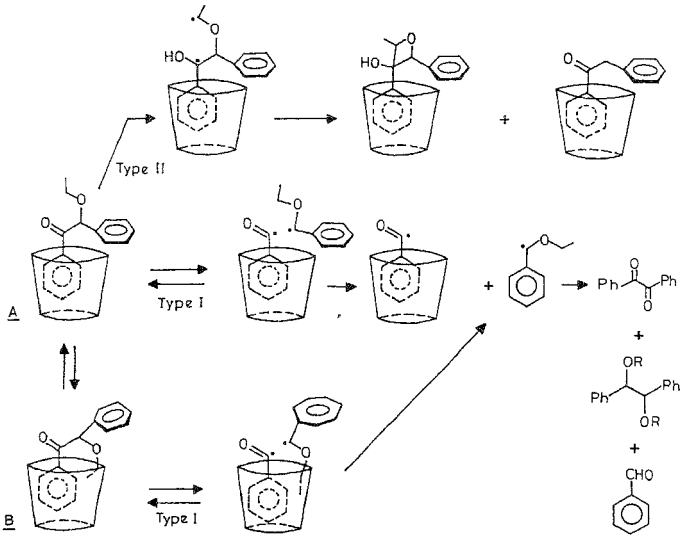

SCHEME 2.

the isolation of type II products in yields > 60%, the rest being starting material. The competitive absorption by one of the photoproducts, deoxybenzoin, acts as an internal filter and slows down the reaction. Therefore, it can be inferred that a majority of the guest molecules are trapped in cyclodextrin with suitable conformation for γ-hydrogen abstraction. In aqueous media, the formation of type II products in minor amounts is attributed to the absence of significant cage effect in solution, even though the molecules (majority) are in favourable conformation for γ-hydrogen abstraction.

4. Long-chain benzoin alkyl ethers (4–6)

The long-chain benzoin alkyl ethers **4–6** behave similar to that of **1–3** in homogeneous media as well as in aqueous cyclodextrin media but differ drastically in cyclodextrin solid complexes. The photolysis of cyclodextrin complexes in the solid state resulted in quantitative yields of benzil and pinacol ethers from type I α-cleavage. Formation of type I products in homogeneous and aqueous cyclodextrin media is expected based on **1–3**. But the formation of the same cannot be explained with the conformational and cage effects. If the conformational and cage effect were operating in these compounds one would not have seen benzol and pinacol ethers. To explain the observed results we invoked a 2:2 complex (Scheme 3).

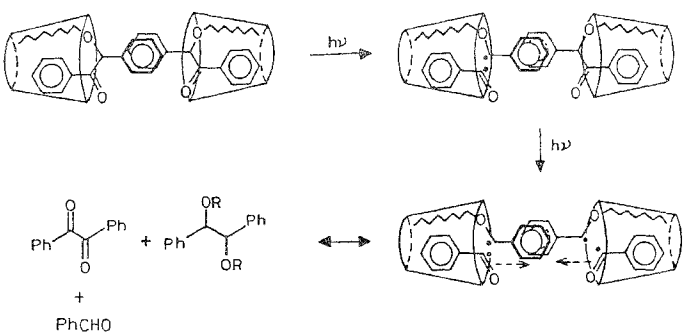

SCHEME 3.

4.1. *Alkyl deoxybenzoins*

The validity of cage effect and conformational effects has been further demonstrated by studying the related systems **7–11**. α-Alkyl deoxybenzoins behave more or less similar to benzoin alkyl ethers in homogeneous or in cyclodextrin complexes.

4.2. *Aryl alkyl ketones*

The aryl alkyl ketones (**12–16**) were chosen to investigate cage effect of cyclodextrin on the partitioning of type II intermediate 1,4-diradical to cyclisation and cleavage. It was anticipated that cyclodextrin cavity would impose certain constraints on product formation from the Norrish type II process which these ketones undergo. The results obtained in the presence of cyclodextrin are compared with the homogeneous results to explain the effect of cyclodextrin. In all the cases, cyclodextrin complexation reduces the yield of the elimination products with respect to *t*-butanol. Further more, a clear trend in elimination/cyclisation is visible when going from **12–16**, the gradual decrease correlating well with the alkyl substituent at γ-position and the influence of cyclodextrin on the product ratio is normally more pronounced in the solid state than in aqueous solution.

As illustrated in Scheme 4, excitation of the aryl alkyl ketones included in the cyclodextrin cavity would result in a 1,4-diradical in which the two singly occupied *p*-orbitals are perpendicular to each other. Since the phenyl group is locked inside the host cavity, the rotation required for further reaction has to occur only on the alkyl side. Rotation of the central C–C bond would result in the *cis*oid-*trans*oid interconversion. It is well established that *in* a medium where the 1,4-diradical is hydrogen bonded, the diradical perfers **3** *trans*oid geometry and therefore elimination products dominate. This is reported to be the case in 4-butanol. Although the internal polarity and the hydrogen-bonding ability of the cyclodextrin cavity would favour the *trans*oid conformation, the hydrophobic effect of the medium would influence the molecule to adopt *cis*oid conformation due to the fact that a part of the molecule (alkyl group) is buried inside the hydrophobic cavity of cyclodextrin along with the phenol ring. A similar structure for the diradical would require the alkyl group to move out of the cavity during the *cis*oid-*trans*oid interconversion. Such a change would be severely restricted since the hydrophobic alkyl chain would prefer to stay in the cavity. On the basis of this model, the contribution of *cis*oid

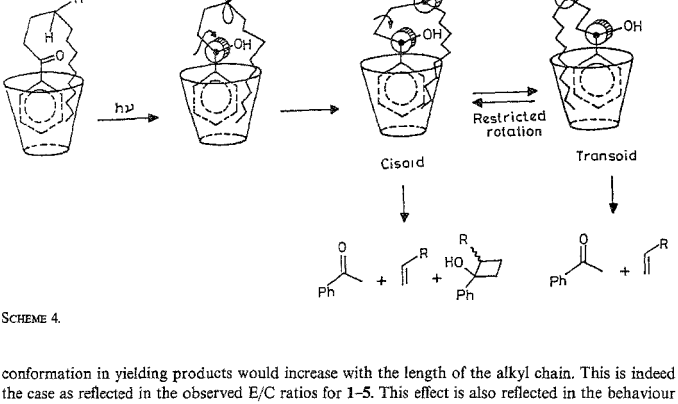

SCHEME 4.

conformation in yielding products would increase with the length of the alkyl chain. This is indeed the case as reflected in the observed E/C ratios for **1–5**. This effect is also reflected in the behaviour of *m*, *para* and *ortho* mythyl octarophenones.

The results presented here clearly illustrate that cyclodextrin cavity can impose restriction on the rotational motions of various single bonds. Such restrictions can often lead to selectivity in product distribution. Examples described here are a testimony to such a phenomenon.

References

1. ATWOOD, J. L., DAVIES, J. E. D. MARNICOL, D. D. (Eds) — *Inclusion compounds*, 1984, Vols 1–3, Academic.
2. RAMAMURTHY, V. — *Tetrahedron*, 1986, **42**, 5753–5839.
3. BENDER, M. L. AND KOMIYAMA, M. — *Cyclodextrin chemistry*, 1978, Springer.
4. LEWIS, F. D., LAUTERBACH, R. T., HEINE, H. G., HARTMANN, W. AND RUDOLPH, H. — *J. Am. Chem. Soc.*, 1975, **97**, 1519–1525.
5. ADAM, S., GUSTEN, H. AND SCHUTE-FROHLINDE, D. — *Tetrahedron*, 1974, **30**, 4249–4255.
6. SANDNER, M. R. AND OSBORN, C. L. — *Tetrahedron Lett.*, 1974, 415–418.
7. HEINE, H. G. — *Tetrahedron Lett.*, 1972, 4755–4758.
8. WAGNER, P. J. — *Acc. Chem. Res.*, 1971, **4**, 168–177.
9. TURRO, N. J., DALTON, J. C., DAWES, K., FARRINGTON, G., HAUTALA, R., MORTON, D., NIEMCZYK, M. AND SCHORE, N. — *Acc. Chem. Res.*, 1971, **5**, 92–101.
10. SCAIANO, J. C. — *Acc. Chem. Res.*, 1982, **15**, 252–258.
11. SCAIANO, J. C. — *Tetrahedron*, 1982, **38**, 819–824.

Thesis Abstract (M.Sc.(Engng))

Studies on bubble formation from closely spaced orifices by Madhup Kumar Singh Solanki.
Research supervisor: T. R. Das.
Department: Chemical Engineering.

1. Introduction

Bubble formation from closely spaced orifices in a filter cloth has been studied primarily to investigate the possibility of developing a rigorous mechanistic mathematical model to predict the final bubble size taking into consideration the phenomenon of coalescence, including the effect of additives on coalescence.

2. Problem formulation

Experiments have been conducted on various types of gas-liquid systems in order to study them mainly with respect to two parameters: (i) average bubble size; (ii) bubble size distribution. Both these parameters have been studied with respect to water as a reference. The effect of additives has also been studied with respect to water as a reference liquid. In each case, however, the gas phase has been air.

A review[1,2] of the existing literature has been made and a critical assessment is presented which follows in short:

(i) No model exists for bubble formation from closely spaced orifices of an 'actual' distributor.
(ii) Even coalescence between two closely approaching bubbles is not thoroughly understood.
(iii) It is not clear how and why electrolytes influence bubble formation. There seems to be more than one mechanism operating.
(iv) There is clearly a need for extensive data with different electrolytes using an 'actual' distributor.

3. Results and discussion

Based on the present studies, it is concluded that with the present state of our understanding of surface and 'local' viscosities in thin-draining liquid films between mobile interfaces and quantitative scales for extent of 'structuring' (the concept of 'structuring' has been introduced from a very basic standpoint in the thesis); it is not possible to develop a mathematical model at present but a hypothesis has been proposed which is able to explain the experimental findings of the present work and very well may be regarded as a precursor to a mathematical model since the hypothesis may be converted to one such model, once we have an understanding of certain aspects related to liquid film drainage.

4. Conclusion

Several workers[3-6] have reported the existence of 'ionic bubbles' in electrolyte solutions but no work up to date deals with a mechanism to which may be ascribed the origin of these bubbles.

The present hypothesis also attempts to explain the mechanism of formation of the 'ionic bubbles' and as a consequence also explains why bubble-size distributions in electrolyte solutions are bimodal in nature.

The present work recognises the liquid film drainage between bubbles as a major process influencing

coalescene and attempts to identify the various possible mechanisms which may play a role in it. These mechanisms involve:

(i) Electrical double layer formation.
(ii) 'Structuring' of the liquid. ('Structuring' may be enhanced by the addition of structure makers and diminuted by the addition of structure breaker.)
(iii) 'Local viscosity'. (This is manifested actually on a microscale but our perception of it is only on a microscale in the form of bulk viscosity.)

Apart from discussing the role of these mechanisms, their mutual interaction has also been considered *i.e.*, what happens when more than one of these mechanisms operate simultaneously.

Since the distributor resembles more closely a 'real' system the problems faced with the filter cloth distributor are also discussed in detail.

References

1. KUMAR, R. AND KULOOR, N. R. — The formation of bubbles and drops, *Advances in Chemical Engineering*, Vol. 8, 1970, pp. 256–368.
2. RAMAKRISHNA, S., KUMAR, R. AND KULOOR, N. R. — Studies in bubble formation-I. Bubble formation under constant flow conditions, *Chem. Engng Sci.*, 1969, **24**, 731–747.
3. TITOMANLIO, G., RIZZO, G. AND ACIERNO, D. — Gas bubble formation from submerged orifices—Simultaneous bubbling from two orifices, *Chem. Engng Sci.*, 1976, **31**, 403–404.
4. IVANOV, I. B., RADOEV, B. P., TRAYKOV, T. TR., DIMITROV, D. ST., MANEV, E. D. AND VASSILIEFF, CHR. ST. — Hydrodynamics of foam and emulsion films, *Proc. Int. Conf. on Colloid and Surface Science*, 15–20 Sept., pp. 583–590, Elsevier, 1975.
5. SARADHY, Y. P. AND KUMAR, R. — Drop formation at sieve plate distributor, *Ind. Engng Chem., Process Des. Dev.*, 1976, **15**, 75–82.
6. FRANK, H. S. AND EVANS, M. W. — Free volume and entropy in condensed systems. III. Entropy in binary liquid mixtures; Partial moral entropy in dilute solutions; Structure and thermodynamics in aqueous electrolytes, *J. Chem. Phys.*, 1945, **13**, 507–532.

Thesis Abstract (M.Sc.(Engng))

A microprocessor-based integrated system for wind tunnel applications by C. Ravikumar.
Research supervisors: V. S. Holla and N. Balakrishnan.
Department: Aerospace Engineering.

1. Introduction

Wind tunnel testing contributes significantly to the design and development of flight vehicles. The electronic measurement and control set-up forms the heart of the wind tunnel facility and is often the major contributing factor that determines the level of sophistication of the facility. The advent of low-cost microprocessors with reasonable computing power has made possible a revaluation of the available instrumentation in wind tunnels. The work reported in this thesis is a contribution in this direction.

The closed-circuit elliptic (7′ × 5′) wind tunnel (CCWT) at the Department of Aerospace Engineering, Indian Institute of Science, is being used for flow field pressure survey and force/moment measurements employing pressure probes and a mechanical balance system. The instrumentation system available at the CCWT before the beginning of this work has been based on classical manual methods resulting in poor turn-around time and error-prone data collection. Upgradation of the system by automation of the experimental procedure eliminates human error in data collection, thus improving the accuracy of the data besides reducing the time for the experiments. Due to the specific acquisition and control functions that are to be implemented in the CCWT, the use of commercially available non-indigenous data acquisition and programmable controllers need extensive tailoring. This often results in poor cost-effective performance. However, the present day's powerful, low-cost microprocessors lend themselves to the inhouse design of efficient application-oriented systems. This has formed the motivation for the present work.

The work reported in this thesis concerns the design, development and implementation of an automatic data-acquisition and control system based on a powerful 16-bit microprocessor for the above tunnel. A 16-bit microprocessor pair, Intel 8086–8087, forms the heart of the system. A set of reliable interfaces and associated subsystems have also been designed and developed. The processor system and the subsystems have been configured to form an interrupt-driven system, so that the processor time can be effectively utilized. A CRT terminal has also been designed and developed for user interaction. The instrumentation has an interface to standard printers for hard-copy output. In order to store the data, a floppy disk controller has been included. A MULTIBUS interface on the central processor board has been provided to handle any further expansion of the system in the future. The capabilities and the versatility of the system have been further enhanced by providing an interface to IBM PC-compatible machines, so that the high-level language-processing capabilities of the personal computer could be fully exploited, specifically for data presentation.

For the selection of the instrumentation, as a first step, a survey of wind tunnel techniques has been made. Based on this, a new cost-effective configuration has been designed for the CCWT[1].

2. 3-D Probe traverse mechanism

The study of the available instrumentation and the experimental techniques, under the present circumstances, has favoured the retention of the 5-hole probe fitted to the 3-D traverse mechanism, for flow field surveys. In order to automate the traverse operations over a wide span of 96 inches, an interface has been developed using a new technique of position sensing effected by counting the number of revolutions of the drive motor. The number of revolutions counted is a measure of the probe displacement. Optical sensors have been used for this purpose. The microprocessor has been used to control the position as per user requirements and it has been exploited to eliminate the common errors associated with induction motors and mechanical gears.

3. 6-Channel digital manometer

A new microprocessor-based 6-channel pressure-measuring device based on a liquid-level manometer has been designed and developed[2]. The device which is an upgraded version of an earlier assembly[3] is capable of measuring pressures in the range of $\pm$ 1000 mm of alcohol with an accuracy of 0.2 mm absolute. The most attractive feature of this medium-speed instrument is that it can read all the six channels simultaneously. The interface designed facilitates the automatic pressure data collection for flow field surveys.

4. 6-Component strain-gauge balance

To facilitate accurate force measurements, the existing mechanical balance system has been replaced by a new model mounting rig to be used with a six-component strain-gauge balance[4]. The strain gauge has also been calibrated[5]. The present and the future experimental needs at the wind tunnel dictate that the data from the strain-gauge balance be acquired at a sampling rate of 1 kHz and a resolution of at least 12 bits. To this end, a 12-bit data-acquisition system has also been incorporated in the instrumentation system.

5. Scanivalve pressure measurement system

In order to cater to the needs of pressure-plotting experiments and wake-pressure surveys, a 48-port scanivalve with an LVDT type pressure sensor has also been included in the system. This pressure sensor's output is also acquired by the data-acquisition system. The data-acquisition system, considering possible future expansions, has been designed to cater to 32 channels of input data.

Powerful hardware will be of little use without appropriate software. In many applications the software development bears a direct relationship to the available hardware. This often leads to a situation wherein an integrated approach that caters, with equal emphasis, to both hardware and software aspects would be needed for a successful design exercise. The software developed in the present work addresses all these aspects.

6. Data acquisition, reduction and associated software packages

The real-time software developed in assembly language initialises, monitors and controls the individual subsystems in order to provide a powerful user-friendly and integrated instrumentation. In the set-up mode, it aids the user with appropriate prompts and help messages. Data validity is checked during the set-up to prevent inadmissible operation. The user inputs the data and the control commands through the CRT terminal to set up the individual instrument modules for the specific experimental requirements. Once the system is configured, the software ensures the required sequence of control operations on individual instruments and the data are collected in real time. The collected data are limit-checked, averaged for improved accuracy and processed. The data storage format on the floppy disc is compatible with standard IBM format. The data can also be transferred on to DEC system 1090 mainframe computer for detailed analysis, if needed.

A contour-plotting package has been developed on an IBM PC-compatible machine in order to aid the user in the visualisation of the flow field for easy interpretation. Besides, routines for tuft grid plots have also been developed.

The entire instrumentation has been validated through measurements on an ogive-nose cylindrical body. Representative color graphics plots of the processed data have also been included.

References

1. RAVIKUMAR, C., BALAKRISHNAN, N. AND HOLLA, V. S. — A microprocessor based system for wind tunnel measurements, *Proc. 12th Intenational Congress on Instrumentation in Aerospace Simulation Facilities*, June 22–25, 1987, Virginia, USA.

2. RAVIKUMAR, C. AND BALAKRISHNAN, N. — A low-cost microprocessor based multiple pressure measuring system, *J. Microcomputer Applic.*, 1986, **9**, 319–326.

3. GOVINDARAJU, S. P., BALAKRISHNAN, N. AND RAVIKUMAR, C. Development of a pressure sensor with digital output based on a liquid manometer, *Proc. 11th National Symposium on Fluid Mechanics and Fluid Power*, December 1982, pp. AP14–19.

4. GOVINDARAJU, S. P. AND HOLLA, V. S. *Design of the pitch and the yaw mechanism for a wind tunnel*, Technical Report No. AE-380/A, Deptt of Aerospace Engng, IISc, Bangalore, 1984.

5. RAVIKUMAR, C., RAMASWAMY, M. A. AND HOLLA, V. S. *Calibration of the six-component strain gauge balance for the CCWT*, Technical Report No. AE-397/A, Deptt of Aerospace Engng, IISc, Bangalore, 1986.

Thesis Abstract (M.Sc.(Engng))

A study of the source-substrate geometry to achieve thickness uniformity of thin films by T. S. Radha Bai.
Research supervisors: E. S. Raja Gopal and A. G. Menon.
Department: Instrumentation and Services Unit.

1. Introduction

Evaporated thin films of metals, dielectrics and combination of the two find many scientific and industrial applications. In most applications at least one of the thin film properties depends on the film thickness, for example, the transmittance and reflectance in optical coatings. For most industrial applications of thin films, it is also important to fabricate a number of components simultaneously in order to save time and cost. It is often required that the film thickness of all the components be the same to have identical physical properties, that is the film thickness be uniform over a large substrate area within $\pm 1\%$. The simpler methods of deposition of thin films by vacuum evaporation do not offer uniform coating on large area. From the simple theory proposed by Holland[1], one can arrive at the approximate thickness of the thin film for a particular configuration of the source and the substrate for a given evaporant mass.

Arrangements of evaporation source and substrate geometry to obtain maximum thickness uniformity have been discussed by various workers. In view of the importance of the optimum utilisation of a vacuum system with respect to material effectivity and also substrate area, this work is undertaken to develop theoretical models for the thickness distribution of thin films on stationary and rotary work holders. An algorithm has been developed to optimise the source-substrate parameters to achieve maximum uniformity both for rotary and stationary work holders.

2. Results and conclusions

To obtain uniform film thickness on a large surface one has to consider the shape of the surface and the arrangement of the evaporation source(s) relative to the surface. It is shown that the thickness at various points on the substrate may be controlled by altering the substrate geometry (spherical or conical). Theoretical distribution curves for stationary spherical and inclined substrate holders indicate the choice of selection of parameters for achieving a particular specification in thickness on small-area substrates. Thickness uniformity of $\pm 15\%$ can be realised by a proper choice of the angle of inclination of the substrate.

From the above results it is seen that the geometry alone is not sufficient to improve the thickness uniformity. It is generally necessary to rotate a substrate to alter the spatial distribution of evaporated

material in order to achieve the desired uniformity of film thickness. Theoretical studies indicate that rotary work holders offer more material effectivity as well as substrate area for a specified uniformity than a stationary system[2] In this work an algorithm is proposed for the optimisation of parameters for achieving maximum uniformity. It has been shown that there exists an optimum geometry of source-substrate position for achieving maximum uniformity both for point and surface sources. An experimental system has been designed and fabricated to check the above results. It is shown that the uniformity of evaporated aluminium thin film choosing the optimum geometry checks well with the theoretical predictions.

As a next logical step, a theoretical model has been proposed to find out the distribution of film thickness on planar substrates using a planetary rotating work holder. The study indicates no further refinement in the thickness uniformity than offerred by a simple rotary system. It is concluded that the only advantage of using a planetary system would be to average out the non-uniformity of the emission characteristics of the source and also to deposit uniform coatings on a number of large substrates. This is achieved if one considers each platen as one rotary substrate and by positioning the platen and the source at the optimum distances for a rotary system as discussed in the algorithm.

Finally, to increase the substrate area of a coating plant rotating spherical work holders are preferred. Theoretical distribution curves for various parameters are presented. It is shown that a large number of small components can be accommodated on the spherical dome and thin films of required uniformity can be deposited with the proper selection of source-substrate geometry. This system has been used continuously for depositing laser mirror coatings on a large number of substrates.

It is evident from the above studies that the evaporated vapour distribution on a substrate can be modulated by changing the geometry of the substrate by intercepting the vapour by introducing stationary masks and by rotating the substrate or mask or by both[3]. Using these principles linearly graded thin metal and dielectric films have been designed and fabricated.

In conclusion one can say that the studies on thickness distribution of thin films can be used to determine the optimum source-substrate geometry to deposit thin films of desired thickness profiles[4].

References

1. HOLLAND, L AND STECKLEMACHER, W. — *Vacuum*, 1952, **11**, 346–364.
2. BEHRNDT, K. H. — *Trans. 10th Vac. Symp.*, 1963, p. 379, Macmillan.
3. RAMSAY, J. V., NETTERFIELD, R. P. AND MUGRIDGE, E. G. V. — *Vacuum*, 1974, **24**, 337–340.
4. ANGENIEUX, J., MASSON, A. AND ROUCHOUSE, Y. — *Opt. Engng*, 1985, **24**, 499–501.

Thesis Abstract (M.Sc.(Engng))

Analytical and experimental studies on photobleaching of laser dye by B. K. Jayalakshmi.
Research supervisors: C. R. Prasad and Prabha Venkatesh.
Department: Mechanical Engineering.

1. Introduction

Dye lasers have unique abilities among lasers being broadly tunable across the near-ultraviolet to near-infrared range and their ability to generate ultrashort pulses[1]. The laser medium in these lasers is also special in that it is in the liquid form. A large number of organic dyes belonging to several families have been found to be suitable for efficient laser action. These lasers also have made a great impact in the fields of spectroscopy, optical engineering, meteorology, atmospheric studies, etc. One serious problem that is encountered during the operation of these dye lasers is that the organic dye undergoes irreversible bleaching on long exposure to the exciting electromagnetic radiation. This bleaching depends on several physical and chemical parameters and influences the efficiency of the dye laser. In order to increase the life of the dye, it is necessary to know the mechanisms of bleaching of the dye and then take steps at controlling and reducing the bleaching rate.

Although a number of experimental studies on photobleaching have been carried out[2-5], due to differences in the experimental conditions, the rates of photobleaching obtained from these studies are not universally valid. A systematic experimental study has been undertaken here for measuring the rate of photobleaching of Rhodamine 590 when it is irradiated with CW pumping by argon laser, pulsed pumping by nitrogen laser and broad-band pumping by flash lamps. The results of these experiments are presented in this thesis. A simple model has been used to calculate the rate of photobleaching for different experimental conditions.

2. Experimental studies

Solutions of the dye Rhodamine 590 (Exciton) in methanol with concentrations ranging from 8×10^{-6} to 10^{-4} moles/l were subjected to laser radiation after being placed in a standard 1-cm-quartz spectrometer cell. The lasers used were an argon ion laser (Spectra Physics model 2020) operating either at 514.5 or 488 nm (0.4 W on either line) and a nitrogen laser (337.1 nm) built in our laboratory. The latter is a conventional Blumline discharge laser with a discharge column enclosed in a perspex enclosure of 50 mm square cross-section. The peak power of the laser was about 24 kW and the pulse width 10 nsec with a pulse repetition rate of 25 Hz. In a third set of experiment, the dye was subjected to flash lamp pumping. For coupling the flash lamp radiation to the dye, the dye cell and the flash lamp are placed at the two foci of a highly polished aluminium elliptic enclosure. A low inductance capacitor (50 μF) charged to 1.2 kV was discharged into the flash lamp.

The number of molecules lost due to photobleaching is determined by measuring the increase in transmittance of the dye in its absorption spectrum. Relative absorption spectra of the dye which has been subjected to radiation and the dye of the same concentration which is not subjected to radiation are taken a number of times during any one series of the experiments. Care was taken to prevent any loss of solvent due to evaporation during the experiment by sealing the cell. The increase in transmittance is then converted into number of molecules bleached.

3. Analytical studies

In order to predict the rate of photobleaching it is necessary to know the detailed mechanism and rate constants of each of the significant steps involved. The general schematic that is representative of photobleaching is

$$T_i + M \xrightarrow{k_{ti}} P_i + Q_i \quad i = 1, 2, \ldots$$

$$S_j + M \xrightarrow{k_{sj}} P_j + Q_j \quad j = 1, 2, \ldots.$$

This schematic presumes that the 1st, 2nd,---excited triplets react with another molecule M (which stands for a solvent molecule, impurity or any other species with which triplet can react irreversibly) to produce products P_i and Q_i. To calculate the rate constants it is necessary to compute the populations of the species S_j and T_i. The general set of rate equations governing the populations of S_0, S_1, T_1 and P are:

$$\frac{d(N_1)}{dt} = -\frac{N_1}{f} - k_{SQ}N_Q N_1 - k_{ST}N_1 - k_{SP}N_1 - \frac{N_1 P}{N_{the}} + W(t)N_0 \tag{1}$$

$$\frac{d(N_T)}{dt} = k_{ST}N_1 - \frac{N_T}{T} - k_{TP}N_T - k_{TQ}N_Q N_T \tag{2}$$

$$\frac{d(N_0)}{dt} = \frac{N_1}{f} + k_{SQ}N_Q N_1 + \frac{N_T}{T} + k_{TQ}N_Q N_T - W(t)N_0 \tag{3}$$

$$\frac{dP}{dt} = \frac{P}{c}\left(\frac{N_1}{N_{th}} - 1\right) - \frac{PN_T}{c^N th}. \tag{4}$$

Analyses for this equation have been attempted by many others [6-8]. Here an iterative technique has been used to solve the coupled rate equations and to evaluate the rate constants for different experimental conditions.

4. Results and discussion

Table I summarises the experimental results of quantum efficiency for different concentrations and wavelengths. The results are of the same order as those obtained by several others.

Table I
Quantum efficiency for different concentrations and wavelengths

Excitation mode	Wavelength of excitation	Quantum efficiency			
		Concentrations (moles/l)			
		8×10^{-6}	10^{-5}	5×10^{-5}	10^{-4}
CW	514.5 nm	1.58×10^{-7}	1.52×10^{-7}	1.21×10^{-7}	0.61×10^{-7}
CW	488 nm	2.74×10^{-6}	2.19×10^{-6}	1.76×10^{-6}	1.02×10^{-6}
Pulsed	337.1 nm	2.08×10^{-2}	1.32×10^{-2}	7.80×10^{-3}	4.48×10^{-3}
Pulsed	Broadband	3.43×10^{-6}	3.56×10^{-6}	6.50×10^{-7}	4.06×10^{-7}

The rate of photobleaching evaluated from computations for CW and pulsed excitation is as follows.

Excitation mode	Wavelength of excitation	Rate of photo-bleaching
CW	514.5 nm	2.41×10^{-2}
CW	488 nm	3.96×10^{-2}
Pulsed	337.1 nm	28.5
Pulsed	Broadband	16.2

The experiments carried out here have clearly indicated that there is a very large increase in the quantum efficiency when the dye is excited by UV radiation as compared to visible sources. It may be due to different mechanisms of photobleaching or photolysis of the solvent or the dye.

The computation of the rate constants for photobleaching shows that the mechanisms for different excitation sources ought to be different in view of the large discrepancies in the rate contants. The experimental and theoretical analyses have pointed out the directions in which the results can be interpreted.

References

1. STOKES, E. D., DUNNING, F. B., STEBBINGS, R. F., WALTERS, G. K. AND RUNDEL, R. D. — *Opt. Commun.*, 1972, **5**, 267–270.
2. IPPEN, E. P., SHANK, C. V. AND DIENES, A. — *IEEE J. Quantum Electronics*, 1971, **7**, 178–179.
3. PRASAD, C. R., YOGANARASIMHA, A. AND VENKATESHAN, S. P. — *Indian J. Phys.*, 1980, **54B**, 24–31.
4. SAHAR, E. AND TREVES, D. — *Opt. Commun.*, 1977, **21**, 20–24.
5. WEBER, J. — *Phys. Lett.*, 1971, **37A**, 179–180.
6. SCHMIDT, W. AND SCHAFER, F. P. — Blitzlampengepumpte farbstofflaser, *Z. Naturforschung*, 1967, **22A**, 1563–1566.
7. KELLER, R. A. — *IEEE J. Quantum Electronics*, 1970, **QE-6**, 411–416.
8. LAWANDY, N. M. — *Appl. Opt.*, 1979, **18**, 189–192.